SOLAR ACTIVE LONGITUDES FROM KODAIKANAL WHITE-LIGHT DIGITIZED DATA

Sudip Mandal[1], Subhamoy Chatterjee[1], and Dipankar Banerjee[1,2]
[1] Indian Institute of Astrophysics, Koramangala, Bangalore 560034, India; sudip@iiap.res.in
[2] Center of Excellence in Space Sciences India, IISER Kolkata, Mohanpur 741246, West Bengal, India

ABSTRACT

The study of solar active longitudes has generated great interest in recent years. In this work we have used a unique, continuous sunspot data series obtained from the Kodaikanal observatory and revisited the problem. An analysis of the data shows a persistent presence of active longitudes during the whole 90 years of data. We compared two well-studied analysis methods and presented their results. The separation between the two most active longitudes is found be roughly 180° for the majority of time. Additionally, we also find a comparatively weaker presence of separations at 90° and 270°. The migration pattern of these active longitudes as revealed by our data is found to be consistent with the solar differential rotation curve. We also study the periodicities in the active longitudes and found two dominant periods of ≈1.3 and ≈2.2 years. These periods, also found in other solar proxies, indicate their relation with the global solar dynamo mechanism.

Key words: Sun: activity – Sun: oscillations – sunspots

1. INTRODUCTION

Sunspots are the features on the solar photosphere, visible in white light. Sunspots show a preferred latitudinal dependence that moves from higher latitude toward the equator with the progress of the 11 year sunspot cycle. This migration pattern of the activity zone is known as the "butterfly diagram." Similar to the preferred latitudinal belt, solar active longitudes refer to the longitudinal locations with higher activity compared to the rest of the Sun. Active longitudes in the past have been studied for solar-like stars (Berdyugina & Tuominen 1998; Rodonò et al. 2000). There have been quite a few studies on the active longitudes, from the observational data as well as from numerical simulations (see Berdyugina 2005 for a complete review).

One of the earliest works on solar active longitudes was published from the Kodaikanal observatory by Chidambara Aiyar (1932). Other notable works were by Losh (1939) and Lopez Arroyo (1961). In recent times, Balthasar & Schuessler (1983) (and references therein) showed a strong correlation between the active longitude and the high-speed solar wind. Most of the previous works showed the existence of an active longitude on smaller timescales of 10–15 Carrington rotations. Using Greenwich sunspot data, Berdyugina & Usoskin (2003) reported the presence of two active longitudinal zones that have been persistent for more than 120 years. These two zones alter their activity periodically between themselves. Apart from this "flip-flop"-like behavior, these authors have also shown that the active longitudes move as a rigid structure, in which the separation between the two active longitudes is roughly a constant value of 180°. Migration of the active longitude in the sunspot was studied by Usoskin et al. (2005); the authors found that the migration pattern is governed by the solar differential rotation. In this work they invoked the presence of a weak nonaxisymmetric component in the solar dynamo theory in order to explain the observed longitudinal patterns. There has been some criticism of these works too. Pelt et al. (2005) have shown that some of the above-quoted results may be an artifact of the methods used to derive them.

Active longitudes have also been discovered in other solar proxies. Solar flares, especially proton flares, are found be associated closely with the active longitude locations (Bumba

& Obridko 1969). Neugebauer et al. (2000) found the existence of preferred longitudes in the near-Earth and near-Venus solar wind data. Analyzing the X-ray flares observed with the NOAA/GOES satellite, Zhang et al. (2007) have shown the presence of active longitudes as well as their migration with time. However, the differential rotation parameters obtained with the X-ray flares were found to be different from those obtained by using the sunspots in Usoskin et al. (2005). Using a combination of Debrecen sunspot data and *RHESSI* data, Gyenge et al. (2016) established a probable dependence of flare occurrence on the active longitudes.

In this paper we use the Kodaikanal white-light digitized data for the first time and revisit the active longitude problem with multiple analysis approaches. In Section 2 we give a brief description of the Kodaikanal data that we have analyzed, using two recognized methods from the literature. In Section 3.1 we describe the rectangular grid method and the results of that. We also study the effect of the sunspot size distribution in this method, as described in Section 3.1.1. The other method, called the "bolometric method," is described in Section 3.2. Periodicities and the migration pattern in the active longitudes are described in Section 4 and in Section 4.1, respectively, followed by a summary and discussion.

2. KODAIKANAL DATA DESCRIPTION

We have used the white-light digitized sunspot data from the Kodaikanal observatory in India. The data period covers more than 90 years, from 1921 to 2011. The original solar images were stored on photographic plates and films and were preserved carefully in paper evelopes. These images have been recently digitized (in 4k × 4k format) by Ravindra et al. (2013). Using a modified STARA algorithm (see Ravindra et al. 2013 for details) on this digitized data, sunspot parameters like area, longitude, and latitude have been extracted by Mandal et al. (2016) (henceforth Paper I). Apart from comparing the Kodaikanal data with data from other observatories, in Paper I we also discussed different distributions in sunspot sizes in latitude as well as in longitude. While detecting the sunspots, images of the detected sunspots were also saved in a binary format. Panel (a) in Figure 1 shows representative full-
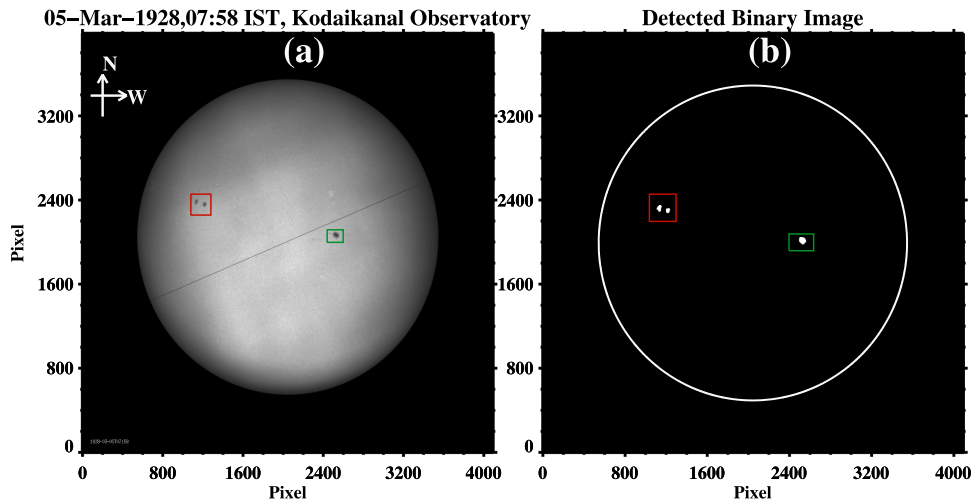
Figure 1. Panel (a) shows a representative image of the Kodaikanal white-light digitized data. The sunspots observed on the image have been highlighted by two rectangular boxes. The binary image of these detected sunspots is shown in Panel (b). The solar limb has been overplotted for better visualization.

disk digitized white-light data. Two rectangular boxes highlight the sunspots present on that day in two hemispheres. The binary image containing these detected sunspots is shown in panel (b) of Figure 1.

2.1. Generation of Carrington Maps

Carrington maps are the Mercator-projected synoptic charts of the spherical Sun in the Carrington reference frame (Harvey & Worden 1998). We have used the daily detected sunspot images (as shown in panel (b) of Figure 1) to construct the Carrington maps. A longitude band of $60°$ ($-30°$ to $+30°$ in heliographic coordinates) is selected for each image to construct these maps (following Sheeley et al. 2011). This involves stretching, B_o angle correction (the B_0 angle defines the tilt of the solar north rotational axis toward the observer, and it can also be interpreted as the heliographic latitude of the observer or the center point of the solar disk), a shift in the Carrington grid, and additions. One Carrington map has been constructed considering a full $360°$ rotation of the Sun in 27.2753 days. In order to correct for the overlaps, we have used the "streak map" (Sheeley et al. 2011) for every individual Carrington map and divided the original maps with them. Data gaps occur as black longitude bands in these maps. The whole procedure is shown in the panels of Figure 2. Here we must emphasize the fact that in our Kodaikanal data we have some missing days (the complete list of missing days has been published with Paper I). In order to increase our confidence in the obtained results, we have not considered any Carrington map in our analysis that has one or more missing days.

3. DATA ANALYSIS

We use the generated Carrington maps for our further analysis. Two different methods, the "rectangular grid" method and the "bolometric curve" method, are used as described in the following subsections. One should note that a possible drift of the active longitudes, due to the differential rotation of the Sun, is not considered here but is analyzed in Section 4.1.
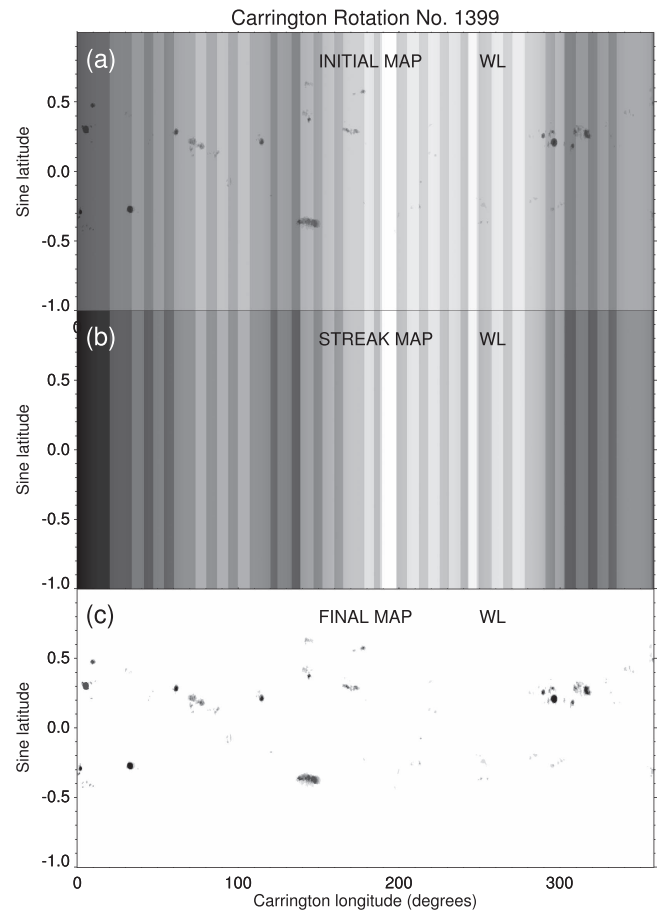

Figure 2. The different steps of producing a Carrington map from Kodaikanal white-light data are shown for a representative Carrington rotation number 1399. Panel (a) shows the original map produced from the binary images. The streak map shown in panel (b) has been used to create the final map (panel (c)) from the original map.

3.1. Using Rectangular Grid

First we follow the "rectangular grid" method (following Berdyugina & Usoskin 2003), where a full Carrington map has been divided into 18 rectangular strips, each of $20°$ longitudinal
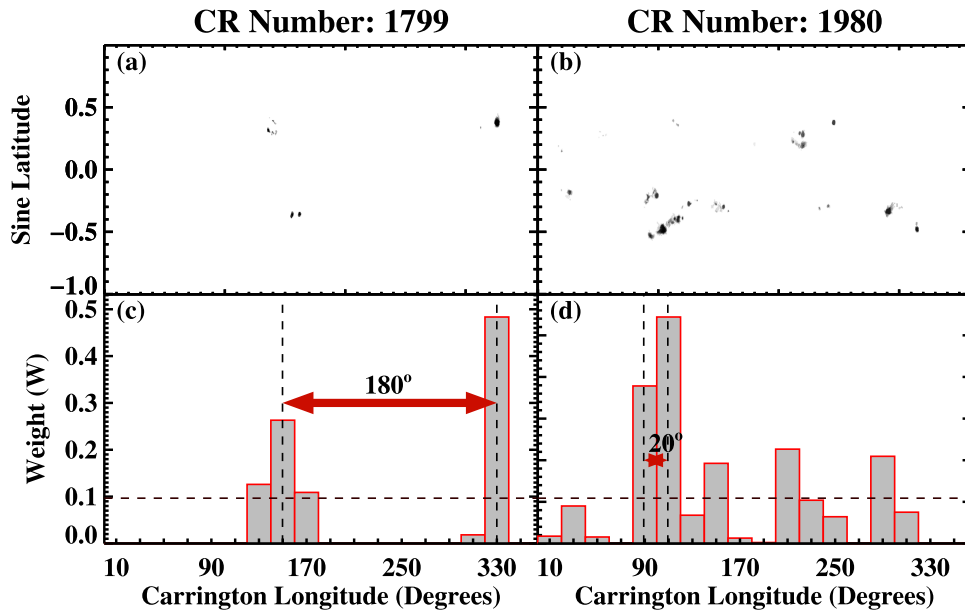
Figure 3. Panels (a) and (b) represent two representative Carrington maps for rotation numbers 1799 and 1980, respectively. Panels (c) and (d) show the weighted value (W) in each longitudinal bin for the two maps. The two horizontal dashed lines represent the cutoff value mentioned in the text. The difference between the two highest peaks in each case is also highlighted in the respective panels.
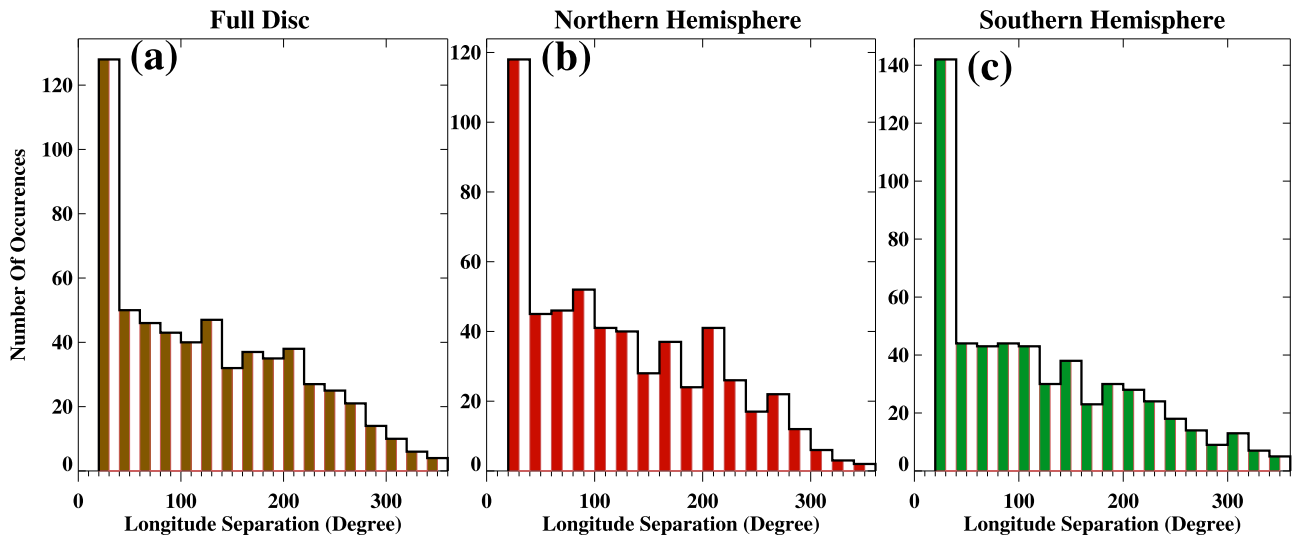

Figure 4. Histograms of the longitudinal difference values between the two most active bins for the full disk and the northern and southern hemispheres.

width. We then compute a quantity "weight" (W) defined as

$$W_i = \frac{S_i}{\sum_{j=1}^{18} S_j} \qquad (1)$$

where S_i is the total sunspot area in the ith bin. We note the longitudes of the highest and the second highest active bins and calculate the separation between them (afterward referred to as "longitude separation"). We impose a minimum of a 20% peak ratio between the second highest and highest peak in order to avoid any sporadic detection. Two such representative Carrington maps from the Kodaikanal white-light data archive are shown in panels (a) and (b) of Figure 3 and their corresponding bar plots in panels (c) and (d). For the two representative cases shown in the figure, we notice that for CR

number 1799 the longitude separation is 180°, whereas for CR 1980 the difference is 20°. We compute such longitude separations for each and every Carrington map for the whole hemisphere (referred to as "full disk" henceforth) and for individual northern and southern hemispheres. Histograms constructed using these separation values for each of the three mentioned cases are shown in different panels of Figure 4. In all three cases (panels (a)–(c) in Figure 4) we see that the maximum occurrence is for the 20° separation. Apart from that, we also notice peaks at ~120° and at ~200° for the full-disk case, whereas these peaks shift a little bit for the northern and southern hemisphere cases. Apart from these mentioned peaks, for the northern and southern hemispheres, we also see weak bumps in the histograms at ~160° and ~270°. In an earlier work using Greenwich data, Berdyugina & Usoskin
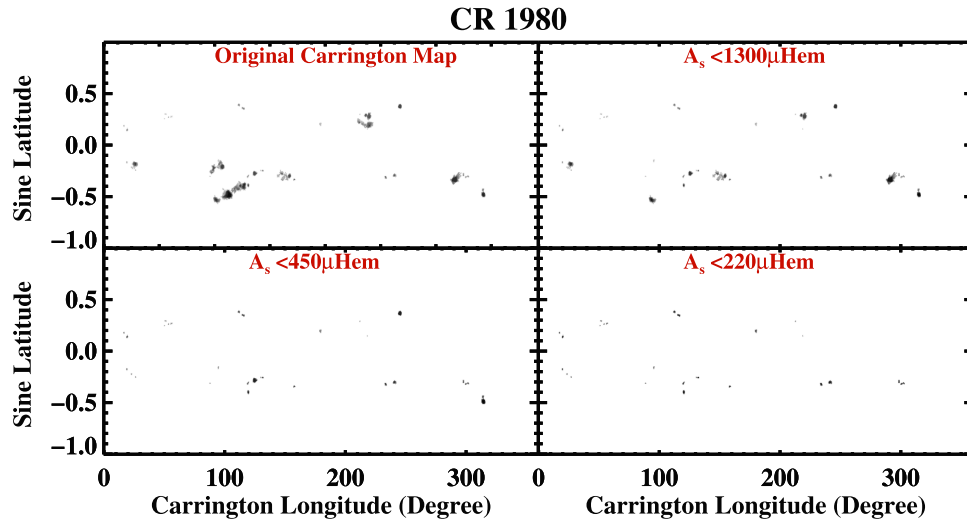
Figure 5. Representation of area-thresholding for CR 1980. Different panels show the area-thresholded maps for different area values (A_s) mentioned in the corresponding panels.
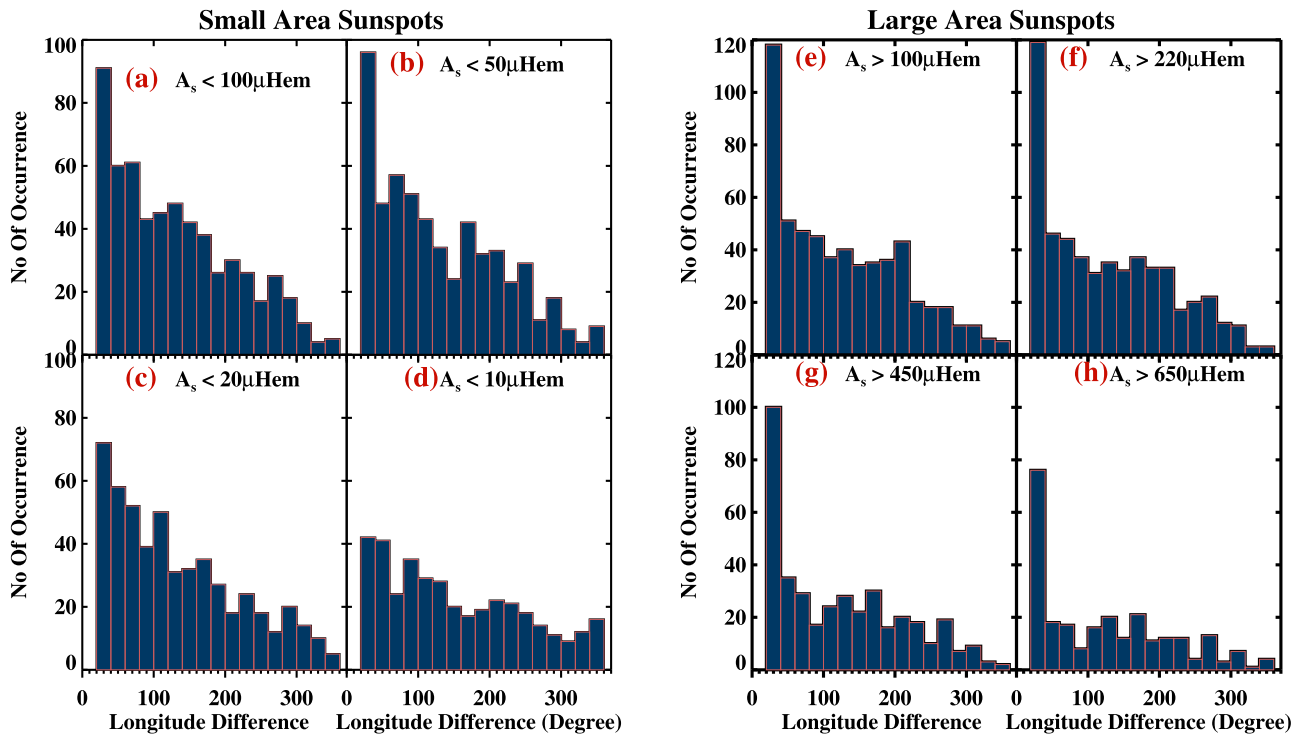

Figure 6. Panels (a)–(d) show the longitude difference histograms for different area-thresholding for the small sunspot areas. Panels (e)–(h) are similar to before but for larger sunspot area-thresholding.

(2003) had reported a phase difference of 0.5 (180° in terms of longitude) between the two most active longitude bins.

The reason for this high number of occurrences of the longitude separations at ∼20° is probably related to the longitudinal extent of the sunspots compared to the chosen bin width of 20°. To be specific, there are often cases when the largest sunspot or sunspot groups are shared by two consecutive longitude bins. Now these occurrences are on a statistical basis, and thus increasing the bin size only shifts the highest peak to the chosen bin value (e.g., for a 40° bin size we find the maximum at 40°). Since this effect is related to the sunspot

sizes, we use area-thresholding on the sunspots and note the longitude separations as described in the next section.

3.1.1. Area-thresholding and Active Longitude

We now use the area-thresholding method on the sunspots found in every Carrington map. One such illustrative example is shown in Figure 5. We again use CR 1980 for demonstration, as it has sunspots of various sizes. Different panels in Figure 5 show the Carrington map before and after doing different area-thresholdings.
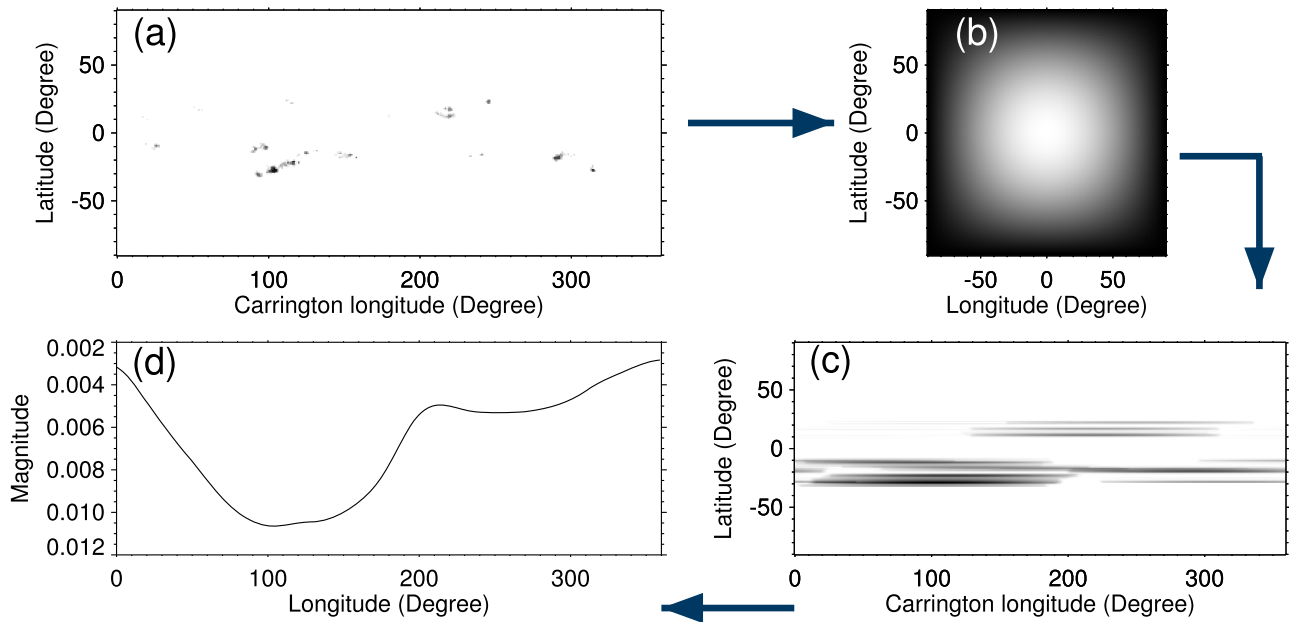
Figure 7. Steps to generate a bolometric magnitude curve starting from a white-light Carrington map as shown in (a). (b) Limb-darkening profile in latitude and longitude; (c) modified Carrington map after shifting (b), multiplying, and adding with (a) along longitude; (d) bolometric magnitude curve generated after adding (c) along latitude normalized by the total of (b). Arrows represent the sequence of bolometric magnitude curve generation.

After performing the area-thresholding, we follow the same procedure as described in the earlier subsection to find the longitude separation between the two most active bins.

Following the extracted sunspot area distribution from the Kodaikanal white-light data (as shown in Figure 7 in Mandal et al. 2016), we chose two kinds of area-thresholding values. The first set of values correspond to sunspots with smaller sizes. These values range from 10 to 100 μHem as shown in panels (a)–(d) in Figure 6. From this figure, we immediately notice that the height of the histogram peak at $\sim$20° decreases progressively with the decrease in sunspot sizes. This is explained by the fact that, as sunspot sizes go down, the probability of a sunspot being shared by two longitude bins is also reduced. This results in a lower peak at $\sim$20°. Also, in every case, we notice prominent peaks in the histograms at $\sim$90° and $\sim$180° separations.

We next investigate the longitude separation for the sunspots with larger sizes. In this case, the thresholding values range from 100 to 650 μHem. In Figures 6(e)–(h) we show the histograms of the longitude difference for these different thresholds. We see two noticeable differences in this case compared to the former one of small sunspot sizes. First, the peak height of the histograms $\sim$20° increases (relative to the other peak heights) as we move toward the larger sunspots, which is expected for the reason we discussed earlier. Along with that we notice that there is no peak near 90° as found earlier, but a peak at $\sim$180° is still present along with other new peaks. Here we should highlight the fact that with higher sunspot area-thresholding, the statistics become poor and the peaks become less significant statistically.

3.2. Using a Bolometric Curve

From our previous analysis we saw that the discreteness introduced by the longitude bins has a definitive effect on the calculated longitude separation. Therefore, we explore the other method, the "bolometric curve" method (Berdyugina &

Usoskin 2003), which produces a smooth curve as described below.

In order to generate the smooth bolometric profile, we first invert the intensities of the Carrington maps to make the white background black with the sunspot as a bright feature. Next, the map is stretched to convert sine latitude into latitude (Figure 7(a)). We then generate a limb-darkening profile with the expression profile $= 0.3 + 0.7\mu$ in latitude and longitude, where μ is the cosine of the heliocentric angle (Figure 7(b)). We then create an intermediate map by shifting the limb-darkening profile, multiplying, and adding with the intensity-inverted Carrington map along every longitude (Figure 7(c)).

In the end, this intermediate map is added along latitude for each longitude to generate a factor, called f. The f curve is converted to a bolometric magnitude curve (m) (Figure 7(d)) using the expression

$$m = -2.5 \log \left[\frac{(1-f)T_{\mathrm{ph}}^4 + f \times T_{\mathrm{sp}}^4}{T_{\mathrm{ph}}^4} \right] \qquad (2)$$

where the bright surface temperature $T_{\mathrm{ph}} = 5750\,\mathrm{K}$ and the sunspot temperature $T_{\mathrm{sp}} = 4000$ K.

Figure 8 shows the two representative plots of this bolometric method. We chose the same two Carrington maps as shown in Figure 3 for easy comparison between the two methods. Now we see that for CR 1799 the bolometric curve basically traces the active bars (as shown in panel (c) of Figure 3); that is, the minimums of the bolometric curve represent the locations of maximum spot concentrations. We notice that the separation in this case (179°) equals the separation obtained previously (180°), but for CR 1980, the difference in this case is $\sim$150°, whereas the previously obtained value was 20°. This is because the bolometric curve takes into account close spot concentrations contradictory to the fixed longitudinal bins as defined in the rectangular grid method. In principle if we smooth out the peaks shown in panel (d) of Figure 3, we should then arrive at a curve similar to the
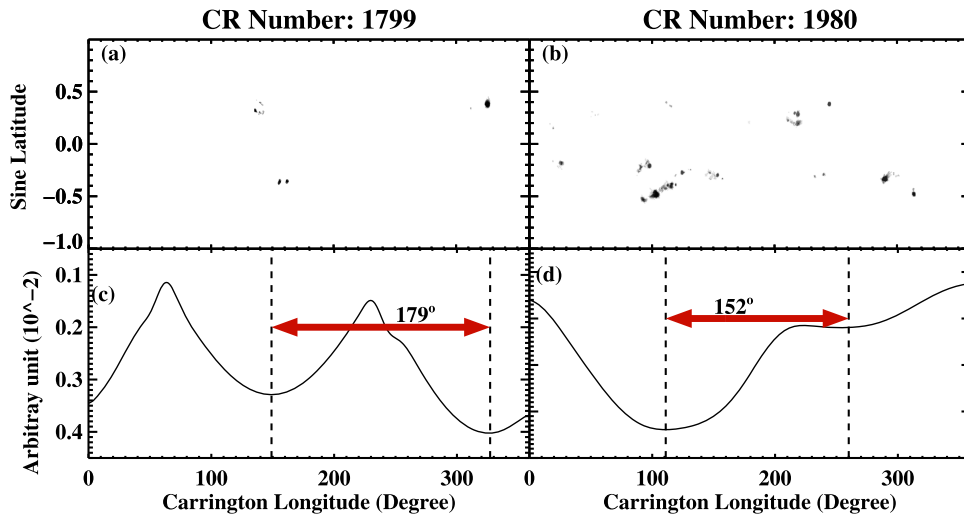
5

Figure 8. Bolometric curves (panels (c) and (d)) for CR 1799 and CR 1980, respectively (panels (a) and (b)). The differences between the longitudes are written in the respective panels.
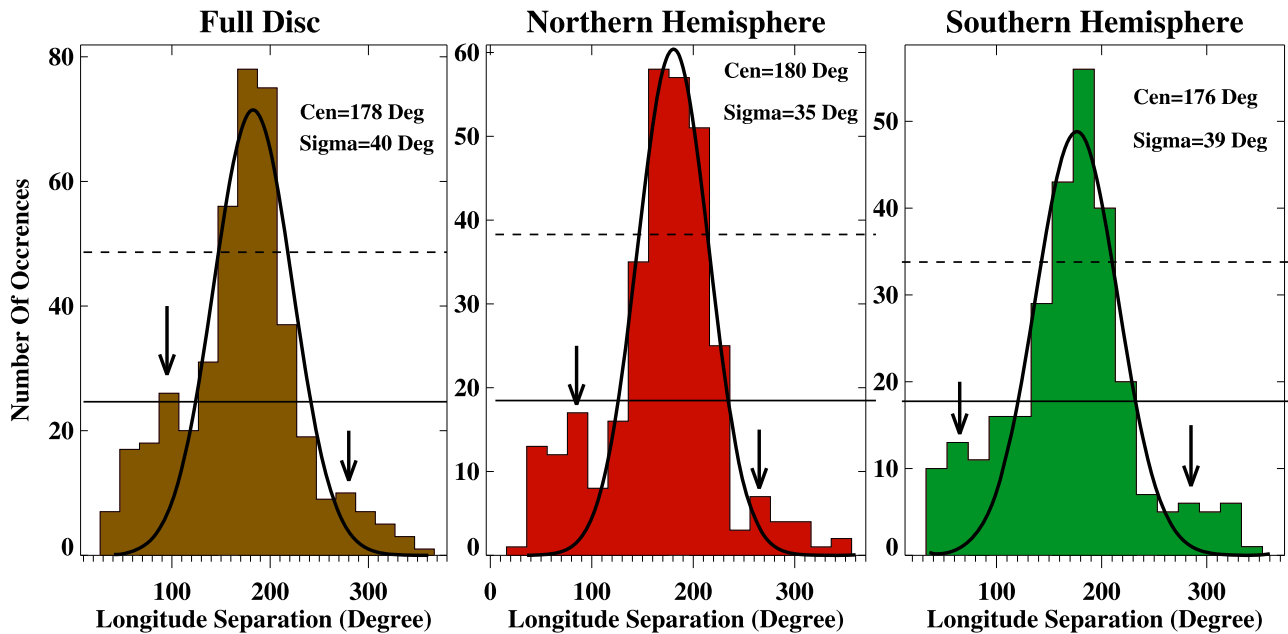

Figure 9. Histograms of the longitude separation computed using the "bolometric curve" method. Fitted Gaussian functions to every histogram are shown as thick black lines. The fitted Gaussian parameters are printed in the corresponding panels. Two black arrows point toward the other two peaks of the histograms located at ~90° and ~270°. Two horizontal lines (solid and dash-dash) represent the mean and the (mean+σ) values, respectively.

bolometric one, but the amount of smoothing is subjective and may be different for different Carrington maps. However, in the case of the bolometric method, we must emphasize that the bolometric curve has been generated using a fixed prescription (Equation (2)) and thus is free from any subjectivity issues. Similar to the earlier method, in this case we have also calculated the longitude separation between the two most active spot concentrations for every Carrington map and plotted the histograms as shown in Figure 9. We can clearly see that for every case (full disk and northern and southern hemispheres) the histograms peak at ~180°. In each case, the histogram distribution looks similar to a bell-shaped curve. We thus fit every distribution with a Gaussian function, as shown by the solid black lines in Figure 9. The centers of the fitted Gaussians for the three cases are at 178°, 180°, and 176°. This agrees well with the results found by Berdyugina & Usoskin

(2003) and Usoskin et al. (2005). Apart from the well-structured peak at ~180°, we also highlight the two other peaks (though considerably weaker) at ~90° and ~270° by two arrows in Figure 9. We remind the reader here that these peaks were also found with the rectangular grid method (Figure 4). These two peaks at ~90° and ~270° probably arise due to the dynamic nature of the active longitude locations. Apart from that, there could also have been some contributions from the different sunspot sizes on the active longitude separations (Ivanov 2007).

Next we investigate the occurrences of the peaks found in Figure 9 for every individual solar cycle (cycles 16–23). The different panels of Figure 10 show the longitude separation histograms for the full period as well as for the individual cycles. We notice that the separation peaks at 180° for every cycle, and the height of this peak follows the cycle
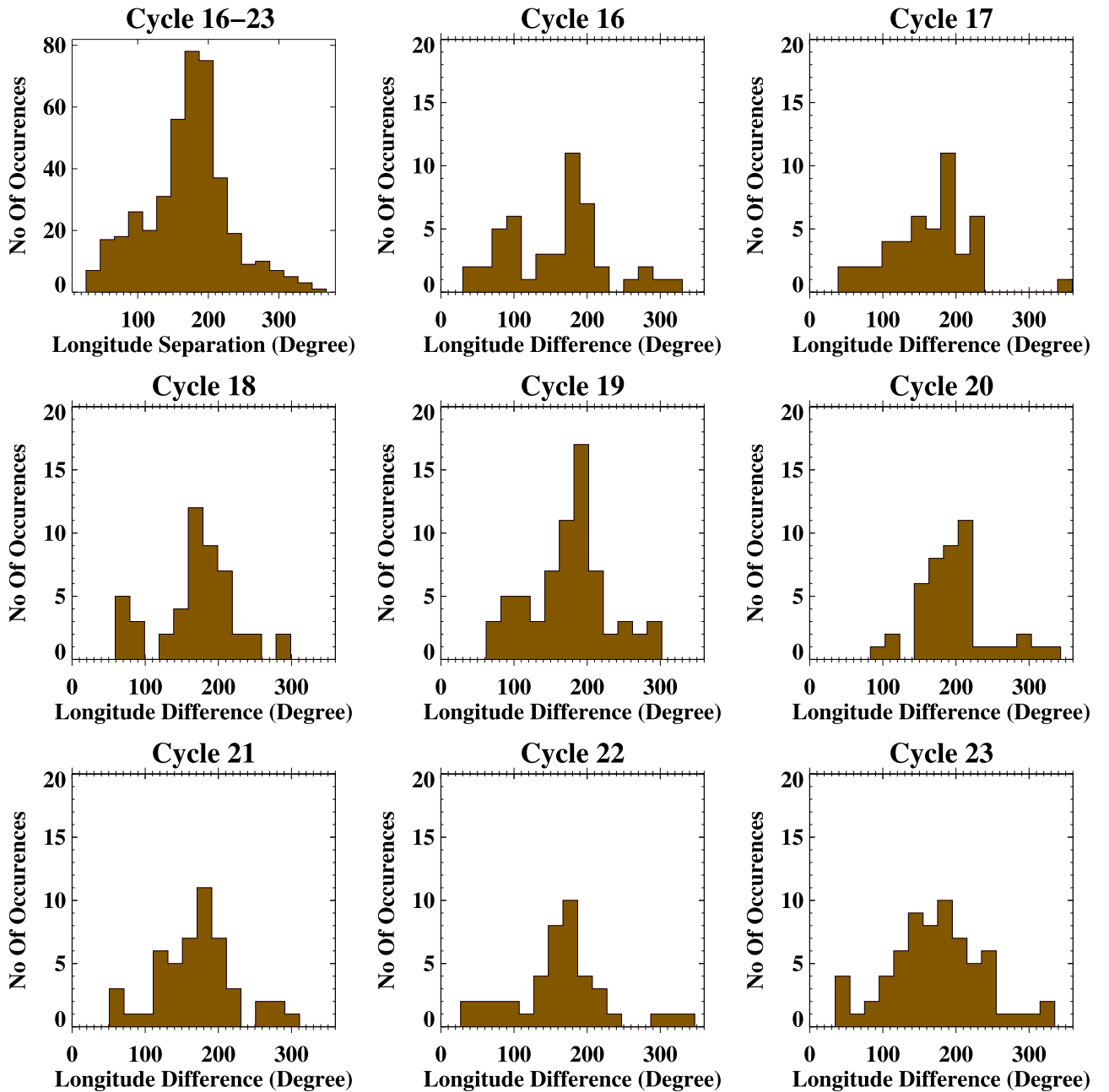
Figure 10. Histograms showing the longitude separation for solar cycles 16–23.

strengths; the strongest cycle, cycle 19 in this case, has the maximum number of occurrences at 180° and so on. Also we notice that the two other peaks (at ∼90° and ∼270°) are also present in most of the cycles, though with lesser strengths. Thus we confirm that these active longitudes persist for the whole 90 years of data analyzed in this paper.

4. PERIODICITIES IN ACTIVE LONGITUDES

Active longitudes have been shown to migrate with the progress of the solar cycle (Usoskin et al. 2005). The activity also switches periodically between the two most active longitude zones (Berdyugina & Usoskin 2003). We investigate the same by using the longitude information of the maximum dip (L_m) using the "bolometric curve" method (for an example, see the 330° longitude of panel (c) of Figure 8). Since we have

rejected any Carrington map that has a data gap (due to missing days in the original Kodaikanal data), we do not have a continuous stretch of L_m for more than 8 years. Figure 11 shows the time variation of the L_m for four different solar cycles for which we have a minimum of 6 years of continuous values of L_m. To smooth out the small fluctuations, we have performed running averaging of 6 months (following Berdyugina & Usoskin 2003). From the plot, we clearly identify periodic variations in every light curve. To get a quantitative estimation of the periods, we use the wavelet tool. The results from the wavelet analysis on the L_m light curves (panels (a)–(d) of Figure 11) are shown in Figure 12. In all these plots, the left panel shows the wavelet power spectrum, and the right panel shows the global wavelet power, which is nothing but the wavelet power at each period scale averaged over time. The 99% significance level calculated for the white noise (Torrence
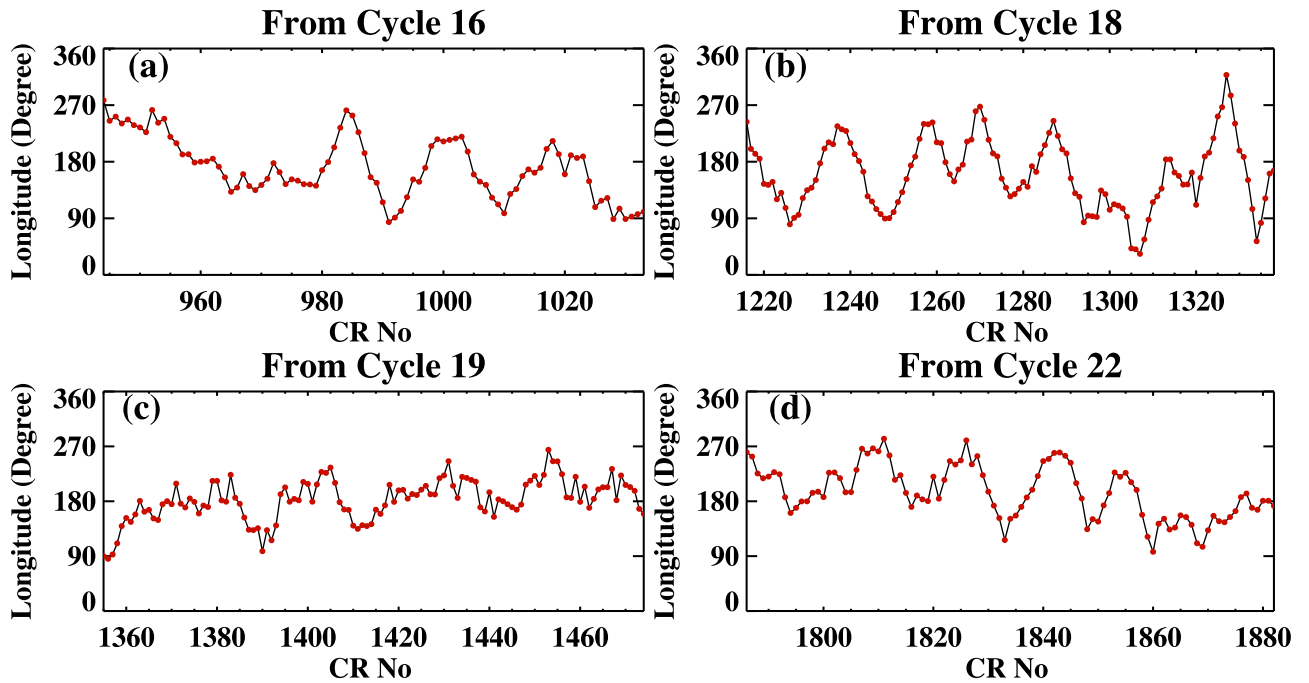
Figure 11. Panels (a)–(d) show the time variation of the longitude of maximum activity, as found from the "bolometric curve" method for four different cycles. A running average of 6 months has been performed to suppress the small fluctuations.

& Compo 1998) has been represented by the contours shown in the wavelet plot and by the dotted line plotted in the global wavelet plot. The effect of the edges represented by the cone of influence (COI) has been shown as the crosshatched region. The periods obtained are indicated in the right-hand side of each plot. Here we must highlight the fact that, due to the shorter time length of the light curves ($\leqslant$9 years), the maximum measurable period in the wavelet (due to COI) is always $\leqslant$3.5 years.

The global wavelet plots indicate two prominent periods of 1.3 years and 2.1 years. This means that the position of the most active bin moves periodically, and these periods persist over all cycles investigated in this case. The occurrence of these two periods is particularly interesting as they have been found using the sunspot area time series from different observatories around the world (Carbonell & Ballester 1990; Krivova & Solanki 2002; Zhan et al. 2006; Mandal et al. 2016). Also, the presence of these periods in all of the cycles again confirms their connection to the global behavior of the solar cycle.

We notice in Figure 11 that there is an average drift of the longitude of maximum activity with the progress of the cycles, and this probably is connected to the solar differential rotation, as explored in the following section.

4.1. Differential Rotation and the Phase Curve

Previous studies have shown that the migration of active longitudes is governed by the solar differential rotation. According to Berdyugina & Usoskin (2003) and Usoskin et al. (2005), the migration pattern can be easily explained if one uses the differential rotation profile suitably. Thus, we move over to a dynamic reference frame defined by solar differential rotation as described below.

The rotation rate of the longitude of activity for the ith Carrington rotation can be expressed as

$$\Omega_i = \Omega_0 - B \sin^2 \langle\theta\rangle_i, \qquad (3)$$

where $\langle\theta\rangle_i$ denotes the sunspot area weighted latitude with Ω_0 and B being $14°.33\,\mathrm{day}^{-1}$ and 3.40, respectively (following Usoskin et al. 2005). Using this rotation rate, the longitudinal position of active longitude in the Carrington frame for the ith rotation (Λ_i) can be calculated from the same at the N_0^{th} rotation (Λ_0) through the relation

$$\Lambda_i = \Lambda_0 + T_C \sum_{j=N_0+1}^{i} (\Omega_C - \Omega_j) \qquad (4)$$

with $\Omega_C = \frac{360°}{T_C}$ and $T_C = 25.38$ days. From the longitudes, the phases are calculated as $\phi = \frac{\Lambda}{360°}$. These phases are made continuous (Figure 13) by minimizing $|\phi_{i+1} + N - \phi_i|$ with N spanning positive and negative integers. Here ϕ_{i+1} is replaced by $\phi_{i+1} + N$ for the N that gives the minimum absolute difference mentioned. We calculate the missing phases to fill the gaps occurring due to missing Carrington maps by interpolating over $\langle\theta\rangle_i$. From Figure 13, we see quite a few distinct features. Immediately we recover the 11 year period of the solar cycle. Also, we see that for an individual cycle the curve first steepens and then dips toward the later half of the cycle. This is explained by considering the fact that, in the beginning of a solar cycle, sunspots appear at higher latitudes where the rotation rate is quite different from the Carrington rotation rate (which is basically the rotation rate at $\approx$15° latitude). As the cycle progress, sunspots move down toward the equator, and the curves then tend to flatten.
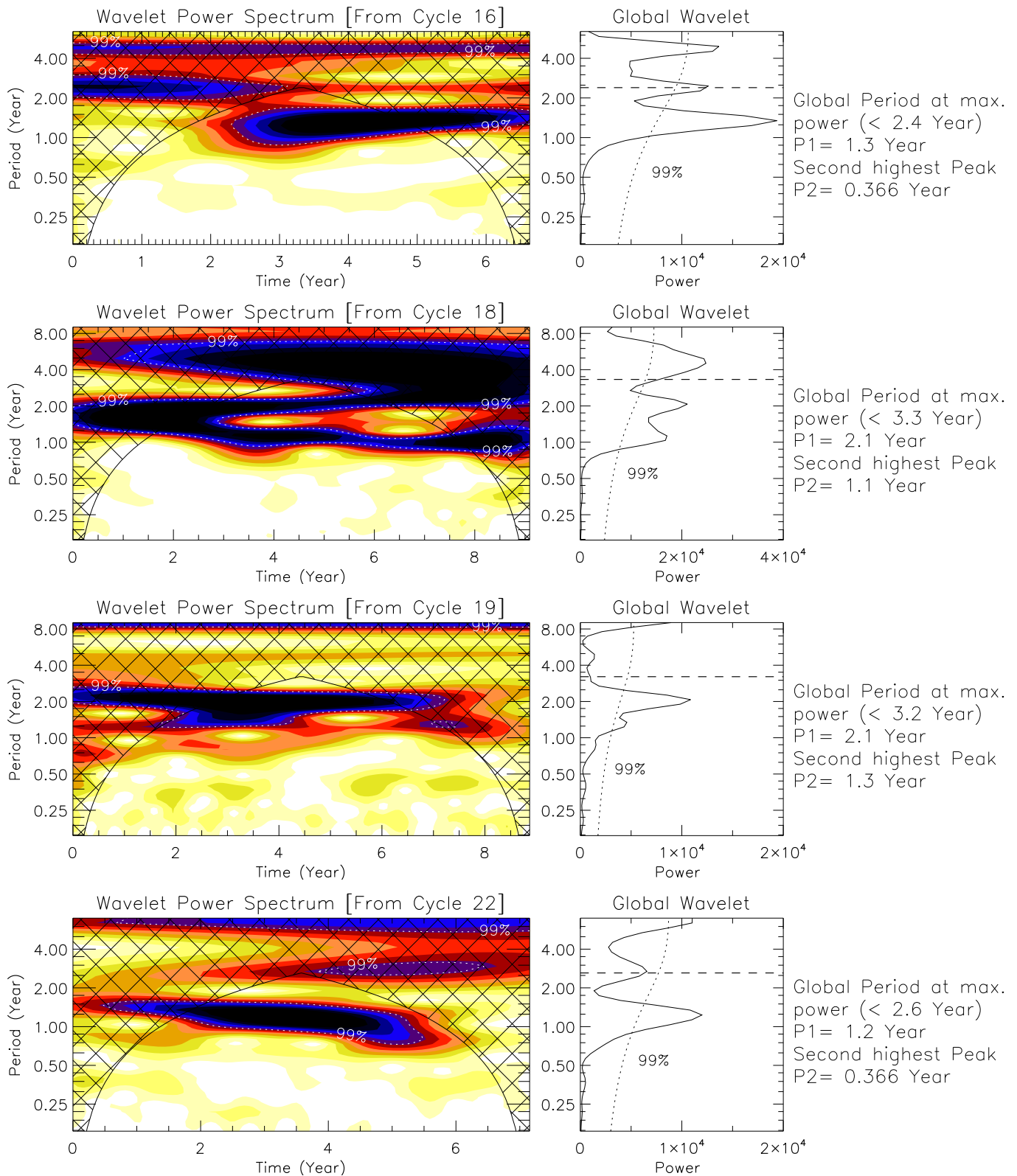
8

Figure 12. Top to bottom: results of wavelet analysis on the light curves shown in panels (a)–(d) of Figure 11, respectively. The periods with the maximum significant powers are listed after the wavelet power spectrum (left panel) and the global wavelet plot (middle panel).

Though we call it a "theoretical curve," we want to remind the reader that the area weighted latitude information is extracted for the generated Carrington maps, and thus it will be appropriate to call it a "data-driven theoretical curve."

We use this "theoretical curve" to demonstrate the association of the migration of the active longitudes with the solar differential rotation. In the top panel of Figure 14 we plot the full-disk bolometric profiles (as obtained previously) and
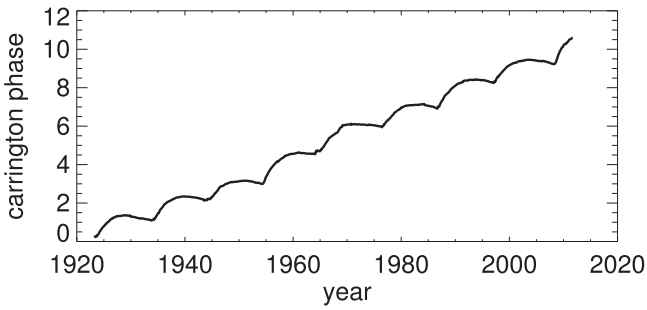
Figure 13. Carrington phase of active longitude as a function of time as derived using Equation (4).
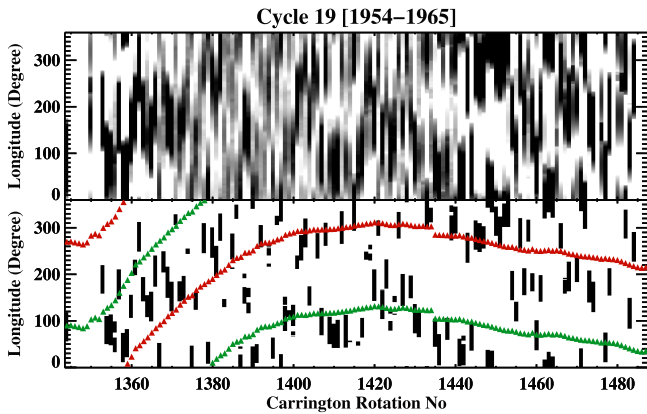

Figure 14. The top panel shows the bolometric profiles stacked over the Carrington rotation period for the 19th cycle. The sigma-thresholded image of the same is shown in the bottom panel. Overplotted red and green symbols indicate the phases obtained using Equation (4).

stack them over the Carrington rotation for the period 1954–1965 (which corresponds to the 19th cycle). The two dark curves are the manifestation of the two dips corresponding to two active longitudes. To highlight this trend more, we use sigma-thresholding (i.e., mean$+\sigma$) on the original image and plotted it in the bottom panel of Figure 14. We then generate the theoretical curves, corresponding to two active longitudes as obtained from each bolometric profile and overplotted them. A good match between the theoretical curve and the obtained active longitude positions confirms the fact that the migration of these active longitudes is indeed dictated by the solar differential rotation. Here we again highlight the fact that the missing phases have been filled using the interpolation method. Since the current phase has contributions from the previous phases (see Equation (4)), we could not match every detail of the observed pattern for all of the cycles. The small discrepancy between the theoretical curve and the data could also be due to the fixed values of the differential rotation parameters used in this study, which may not be suitable for all cycles.

5. SUMMARY AND CONCLUSIONS

In this paper, in the context of active longitude, we have analyzed, for the first time, the Kodaikanal white-light digitized data that cover cycles 16–23. We have analyzed the data with two previously known methods, the "rectangular grid" method and the "bolometric curve" method, for the full disk as well as

for the individual hemispheres. Below we summarize the key findings from our analysis:

1. From the two methods, we see that for the entire duration of the data analyzed, we find two persistent longitude zones or "active longitudes" with higher activity. This is consistent with the results from the Greenwich data as obtained by Berdyugina & Usoskin (2003).

2. Using the "rectangular grid" method, we have constructed the histograms of the longitude separation between the two active longitudes and found prominent peaks in the histograms at $\sim90°$, $\sim180°$, and $\sim270°$. We also noted that the highest peak occurs for the separation of 20°. We use area-thresholding on the sunspots to show that the peak at 20° is due to the presence of relatively large sunspots being shared by two consecutive longitude bins.

3. Using the bolometric method, we recover the peaks at $\sim90°$, $\sim180°$, and $\sim270°$ as found earlier. Also, we find that the peak height for the 180° separation is much higher than the other two peaks. We fitted the central lobe with a Gaussian function and estimated the center location. Applying this method for individual solar cycles, we established that the peak at 180° is always present in every solar cycle.

4. Using temporal evolution of the peak location of highest activity, we have demonstrated the presence of two periods using the wavelet analysis. The two prominent periods are 1.1–1.3 years and 2.1–2.3 years. These two periods are routinely found in the sunspot area and sunspot number time series. Apart from that, we also observe another period of ~5 years with significant power. Due to the shorter length of the time series, this period is beyond the detection confidence level. However, the presence of the period directly indicates its connection with the global solar dynamo mechanism, which needs to be investigated further.

5. Finally, we use the solar differential rotation profile to construct a dynamic reference frame. A theoretical curve has been generated using area weighted sunspot latitude information from the Carrington maps. While overplotting this curve on top of the sigma-thresholded image of the bolometric profiles, we have shown that the migration pattern follows the solar differential rotation, as found in some previous studies.

To conclude, we found signatures of persistent active longitudes on the Sun using the Kodaikanal data. We hope that with these observational results along with the solar models, the understanding of the physical origin of active longitudes can be advanced.
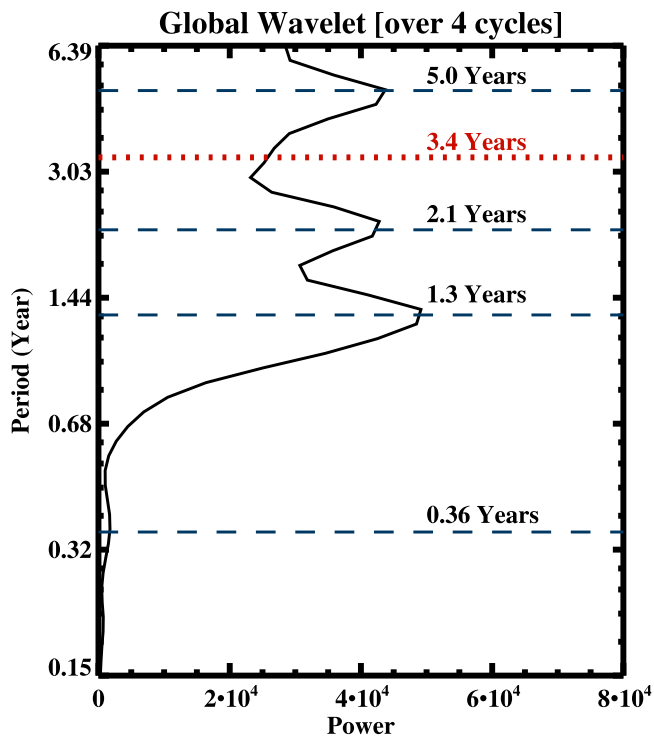
Figure 15. The global wavelet power summed over four cycles (cycles 16, 18, 19, and 22). The red dotted line indicates the maximum measurable period due to the COI.

APPENDIX

We explore the global nature of the periods found in Section 4 by summing up the wavelet power over four cycles (cycles 16, 18, 19, and 22). In Figure 15 we show the summed-up

power with the calculated periods. Three periods (0.36 years, 1.3 years, and 2.1 years) are within the maximum measurable period of 3.4 years. From the plot we notice that the power is mostly concentrated on the 1.3 year and 2.1 year periods, whereas very little power is present at the 0.36 year period. We should highlight here the fact that a substantial amount of power is seen at the ~5 year period, but due to the length of the signal it falls outside the maximum measurable period limit.

REFERENCES

Balthasar, H., & Schuessler, M. 1983, SoPh, 87, 23
Berdyugina, S. V. 2005, LRSP, 2, 8
Berdyugina, S. V., & Tuominen, I. 1998, A&A, 336, L25
Berdyugina, S. V., & Usoskin, I. G. 2003, A&A, 405, 1121
Bumba, V., & Obridko, V. N. 1969, SoPh, 6, 104
Carbonell, M., & Ballester, J. L. 1990, A&A, 238, 377
Chidambara Aiyar, P. R. 1932, MNRAS, 93, 150
Gyenge, N., Ludmány, A., & Baranyi, T. 2016, ApJ, 818, 127
Harvey, J., & Worden, J. 1998, in ASP Conf. Ser. 140, Synoptic Solar Physics, ed. K. S. Balasubramaniam, J. Harvey, & D. Rabin (San Francisco, CA: ASP), 155
Ivanov, E. V. 2007, AdSpR, 40, 959
Krivova, N. A., & Solanki, S. K. 2002, A&A, 394, 701
Lopez Arroyo, M. 1961, Obs, 81, 205
Losh, H. M. 1939, POMic, 7, 127
Mandal, S., Hegde, M., Samanta, T., et al. 2016, arXiv:1608.04665
Neugebauer, M., Smith, E. J., Ruzmaikin, A., Feynman, J., & Vaughan, A. H. 2000, JGR, 105, 2315
Pelt, J., Tuominen, I., & Brooke, J. 2005, A&A, 429, 1093
Ravindra, B., Priya, T. G., Amareswari, K., et al. 2013, A&A, 550, A19
Rodonò, M., Messina, S., Lanza, A. F., Cutispoto, G., & Teriaca, L. 2000, A&A, 358, 624
Sheeley, N. R., Jr., Cooper, T. J., & Anderson, J. R. L. 2011, ApJ, 730, 51
Torrence, C., & Compo, G. P. 1998, BAMS, 79, 61
Usoskin, I. G., Berdyugina, S. V., & Poutanen, J. 2005, A&A, 441, 347
Zhan, L.-s., He, J.-m., Ye, Y.-l., & Zhao, H.-j. 2006, ChA&A, 30, 393
Zhang, L., Cui, Y., He, Y., et al. 2007, AdSpR, 40, 970